TDP-43 α-helical structure tunes liquid–liquid phase separation and function

Alexander E. Conicella[a,b,c,1], Gregory L. Dignon[d,e,1], Gül H. Zerze[d,f], Hermann Broder Schmidt[g], Alexandra M. D'Ordine[b], Young C. Kim[h], Rajat Rohatgi[g,i], Yuna M. Ayala[j], Jeetain Mittal[d,2], and Nicolas L. Fawzi[a,2]

[a]Department of Molecular Pharmacology, Physiology, and Biotechnology, Brown University, Providence, RI 02912; [b]Graduate Program in Molecular Biology, Cell Biology, and Biochemistry, Brown University, Providence, RI 02912; [c]Department of Chemistry, University of Toronto, Toronto, ON M5S 1A8, Canada; [d]Department of Chemical and Biomolecular Engineering, Lehigh University, Bethlehem, PA 18015; [e]Laufer Center for Physical and Quantitative Biology, Stony Brook University, Stony Brook, NY 11794; [f]Department of Chemical and Biological Engineering, Princeton University, Princeton, NJ 08540; [g]Department of Biochemistry, Stanford University School of Medicine, Stanford, CA 94305; [h]Center for Materials Physics and Technology, Naval Research Laboratory, Washington, DC 20375; [i]Department of Medicine, Stanford University School of Medicine, Stanford, CA 94305; and [j]Edward Doisy Department of Biochemistry and Molecular Biology, Saint Louis University School of Medicine, St. Louis, MO 63103

Edited by Arup K. Chakraborty, Massachusetts Institute of Technology, Cambridge, MA, and approved February 3, 2020 (received for review July 12, 2019)

Liquid–liquid phase separation (LLPS) is involved in the formation of membraneless organelles (MLOs) associated with RNA processing. The RNA-binding protein TDP-43 is present in several MLOs, undergoes LLPS, and has been linked to the pathogenesis of amyotrophic lateral sclerosis (ALS). While some ALS-associated mutations in TDP-43 disrupt self-interaction and function, here we show that designed single mutations can enhance TDP-43 assembly and function via modulating helical structure. Using molecular simulation and NMR spectroscopy, we observe large structural changes upon dimerization of TDP-43. Two conserved glycine residues (G335 and G338) are potent inhibitors of helical extension and helix–helix interaction, which are removed in part by variants at these positions, including the ALS-associated G335D. Substitution to helix-enhancing alanine at either of these positions dramatically enhances phase separation in vitro and decreases fluidity of phase-separated TDP-43 reporter compartments in cells. Furthermore, G335A increases TDP-43 splicing function in a minigene assay. Therefore, the TDP-43 helical region serves as a short but uniquely tunable module where application of biophysical principles can precisely control assembly and function in cellular and synthetic biology applications of LLPS.

liquid–liquid phase separation | NMR spectroscopy | protein interactions | molecular simulation

RNA-binding proteins harboring low-complexity sequences are significant constituents of membraneless organelles, particularly ribonucleoprotein (RNP) granules (1–3). These granules can display liquid-like properties (4), consistent with the view that they assemble through liquid–liquid phase separation (LLPS) (5). The molecular interactions and physical forces by which RNP granule proteins assemble into liquid-like compartments have been of great interest (6–13). Much work has demonstrated that weak multivalent interactions based on several interaction modes such as electrostatic interactions, hydrogen bonds, cation–π interactions, and other interactions, including sp^2-hybridized groups (14–18), drive this LLPS. Furthermore, LLPS may also be facilitated through specific or nonspecific interactions involving partially ordered domains or fully ordered globular domains (often in modular chains) binding protein or nucleic acid polymers (2, 19–21). This diversity of interaction types mediating LLPS could, in principle, allow for different responses to stimuli, as well as variations in permeability, dynamics, and persistence, thus allowing comparable diversity in their respective biological functions (22–25). However, the biological rules for governing interactions that lead to phase separation and function remain incompletely understood.

TDP-43 (26–29), a well-known component of RNP granules, is a heterogeneous ribonucleoprotein (hnRNP) family member with genetic and/or histopathological links to amyotrophic lateral sclerosis (ALS) (30), frontotemporal dementia (31), and Alzheimer's disease (32). TDP-43 comprises a folded N-terminal domain that is associated with oligomerization (21), tandem RRM (RNA-recognition motif) domains that recognize UG-rich sequences found near RNA splice sites (1), and an extended C-terminal domain (CTD), which is primarily disordered (33, 34) (Fig. 1*A*). The CTD is rich in polar and aromatic residues, is prone to self-assembly, and confers TDP-43 the ability to undergo LLPS both in vitro (33) and in cells (35); intermolecular interactions mediated by the folded N-terminal domain further enhance TDP-43 LLPS and function (21). In addition to the tandem RRMs, the splicing function of TDP-43 also depends on the N- and C-terminal domains (21, 36–40). Notably, an evolutionarily conserved, partially α-helical subregion (conserved region [CR]) of the CTD spanning residues 320–343 is demonstrably important to the ability of TDP-43 to phase separate (33), is required for in cell LLPS of TDP-43 reporter constructs (35),

Significance

TDP-43 is an essential RNA-binding protein that assembles into protein inclusions in >95% of cases of amyotrophic lateral sclerosis (ALS). A partially helical region in the predominantly disordered C-terminal domain harbors several mutations associated with ALS and is important for TDP-43 function and liquid–liquid phase separation. We directly demonstrate that this helical region undergoes large structural changes upon helix–helix dimerization and that point mutations can enhance helix–helix assembly. Furthermore, we demonstrate that these point variants can be used to control the material properties of phase-separated TDP-43 constructs in cells and can enhance TDP-43 RNA-splicing function. Therefore, engineered forms of the TDP-43 helical domain could be used to control in-cell phase separation, dynamic assembly, and function.

Author contributions: J.M. and N.L.F. conceived of research; A.E.C., G.L.D., G.H.Z., H.B.S., A.M.D., Y.M.A., and N.L.F. performed research; Y.C.K. contributed new reagents/analytic tools; A.E.C., G.L.D., G.H.Z., H.B.S., R.R., Y.M.A., J.M., and N.L.F. analyzed data; A.E.C., G.L.D., J.M., and N.L.F. wrote the paper; and H.B.S., R.R., Y.M.A., J.M., and N.L.F. supervised research.

The authors declare no competing interest.

This article is a PNAS Direct Submission.

Data deposition: The NMR chemical shift assignments reported in this paper have been deposited in the Biological Magnetic Resonance Data Bank (BMRB), http://www.bmrb.wisc.edu/ (TDP-43 CTD G335A [27750], G335N [27788], G335S [27789], G338A [27790], and G335D [50090]).

[1]A.E.C. and G.L.D. contributed equally to this work.

[2]To whom correspondence may be addressed. Email: jeetain@lehigh.edu or nicolas_fawzi@brown.edu.

This article contains supporting information online at https://www.pnas.org/lookup/suppl/doi:10.1073/pnas.1912055117/-/DCSupplemental.

First published March 4, 2020.

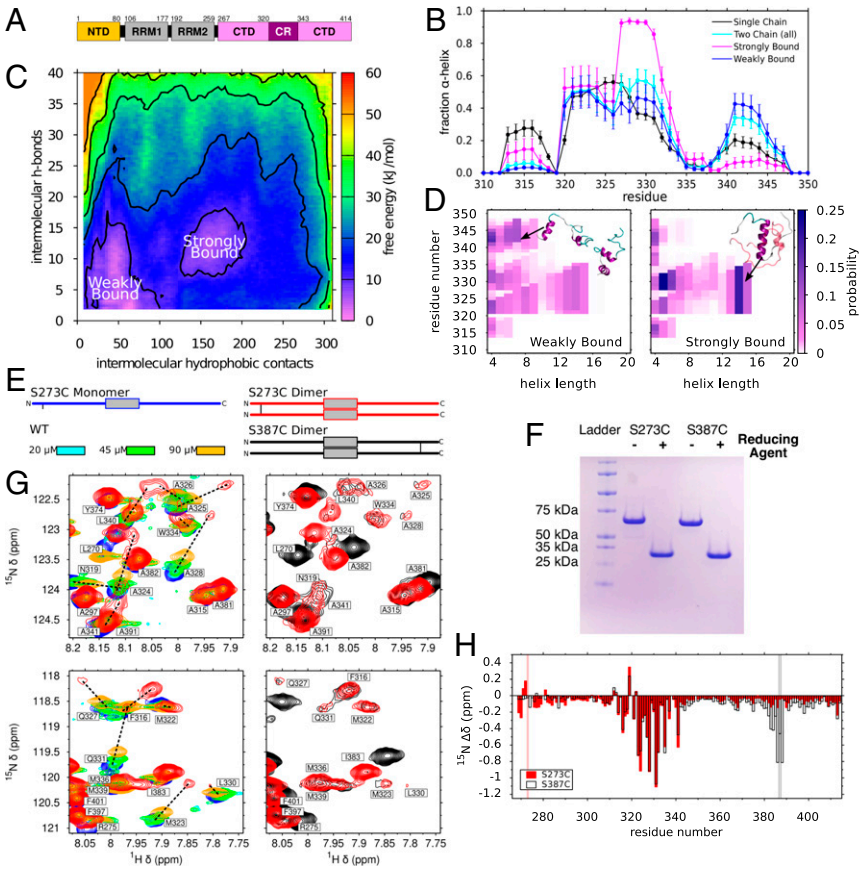

Fig. 1. TDP-43 CTD self-associates and forms transient helical structures. (*A*) Domain structure of TDP-43. (*B*) α-Helical content of TDP-43 simulations at each residue, where single chain comes from a separate simulation of a single TDP-43$_{310–350}$ chain (single chain, black), and the other three curves from a two-chain simulation using all frames (two chain [all], cyan), only strongly bound frames (strongly bound, magenta), or only the weakly bound frames (weakly bound, blue). Data are plotted as mean ± SEM of $n = 5$ equal divisions of the total dataset. (*C*) Free energy landscape of TDP-43$_{310–350}$ intermolecular contacts for all-atom two-chain simulations highlight two minima corresponding to strongly and weakly bound states. (*D*) α-Helical secondary-structure propensity maps show the contribution of all helical configurations to the overall helical content shown in *B*. This analysis highlights stabilization of contiguous α-helical structure in the strongly bound state. (*E*) Schematic of cross-linked CTD variants. (*F*) Nonreducing SDS/PAGE of dimeric S273C and S387C illustrate an apparent reduction of molecular weight by approximately one-half upon addition of disulfide-breaking reducing agent (1 mM DTT). (*G*, *Left*) Select regions from ^{1}H–^{15}N TROSY spectra of dilsulfide-linked homodimeric TDP-43 CTD S273C (red) show line broadening and large upfield ^{15}N chemical shift differences in 321–343 region compared to monomeric reduced S273C (blue), consistent with formation of structure. Chemical shifts for residues in the dimer state were assigned by extrapolation (dashed black line) from spectra of 20 μM (cyan), 45 μM (green), and 90 μM (orange) WT. (*G*, *Right*) Overlay of ^{1}H–^{15}N TROSY spectra regions for homodimeric S273C and S387C are similar in the central 320–340 region. (*H*) Quantification of ^{15}N Δδ values between homodimeric S273C (red) and S387C (black) and their respective monomers. The gray boxes indicate the positions of S273C and S387C disulfide cross-links.

and is essential for TDP-43 splicing-associated function in a well-established minigene assay (41). The importance of the CR to TDP-43 function is underscored by the presence of seven ALS-associated variants in this short stretch (41).

Previously, we showed that the conserved TDP-43 CTD region mediates intermolecular α-helical contacts enhancing TDP-43 phase separation (33). In particular, a transiently helical region spanning 321–330 (34) is stabilized and extends into the adjacent 331–343 region upon self-association (33). However, we were previously not able to directly trap and quantify the extent of the helical stabilization of TDP-43 upon assembly. Importantly, we found that several ALS-associated missense mutations in this region (including Q331K and M337V) disrupt helix–helix interaction, impairing phase separation (33). Intriguingly, the adjacent 331–343 region that becomes partially helical upon assembly contains two nearby conserved glycine positions, G335 and G338. Because the inclusion of designed helical regions has been recently demonstrated to enhance protein phase separation (42), we suspected that these "helix-discouraging" glycine residues might serve as important sites regulating TDP-43 assembly. Therefore, we set out to demonstrate that the region undergoes a significant change in structure upon assembly and to test whether TDP-43 helical structure and helix–helix interaction can be tuned to enhance phase separation and increase TDP-43 function by α-helix enhancing mutations at conserved glycine positions.

In this work, we use experiments and simulations to characterize the helical structure of the dimeric form of the TDP-43 CTD and the influence of two nearby glycine positions on TDP-43 CTD structure, self-association, phase separation in vitro and in cells, and splicing function. We also test the effect of the G335D ALS-associated mutation occurring at one of these sites to understand how the protein phase separation and splicing function is perturbed by changes in the underlying helix propensity, which may provide insight into potential mechanisms leading to disease (43). Here, we pair an extensive experimental and computational structural and biophysical characterization of TDP-43 CTD, including several mutants targeted at these two glycine residues with an evaluation of the role of these positions on TDP-43 LLPS and splicing function in cells. The combination of high-resolution NMR spectroscopic and computational structural data, phase separation approaches in vitro and in cells, and functional data provide a

comprehensive, atomically detailed picture of the tuning of phase separation by single position substitutions. Looking ahead, the tunable interactions of this short segment could be broadly applied to control structure, interactions, and both phase separation and function.

Results

Helical Structure of TDP-43 CTD Enhanced by Dimerization. Our previous work showed that the CR in TDP-43 CTD (residues 320–343) contains a segment from 321 to 330 that is partially helical and that helicity is enhanced in 321–330 and spreads to 331–343 upon TDP-43 self-interaction (33). However, despite the importance of the CR in TDP-43 splicing function (40) and phase separation (33, 35), the precise extent of increased α-helicity and structural change in the assembled state remains poorly understood. Because we could not trap the assembled state, we previously relied on experiments sensitive to the small population of the assembled state (chemical shift deviation vs. concentration, and relaxation dispersion NMR) present in equilibrium with the monomeric state. Signs of enhanced helicity were present, but direct characterization of the size and extent of helicity in the assembled form could not be achieved (33). Here, to directly visualize the structural changes along the self-assembly pathway, we first used all-atom explicit solvent simulations. Using advanced sampling techniques (*Methods*) (33), we determined the equilibrium ensemble of configurations of two copies of a computationally tractable segment of TDP-43 CTD, TDP-$43_{310–350}$, containing the entire helical region placed together in a simulation box. First, we found that overall α-helical content [as calculated by the dictionary of secondary structure of proteins (DSSP) (44)] for the entire two-chain ensemble (i.e., including configurations with and without intermolecular contacts) remains ∼50% in the partially helical region spanning 321–329 but helicity increases in the region from 330 to 334, up to 60% helical for the two-chain simulation compared to 40% helical for the single chain (Fig. 1*B*). Importantly, this 330–334 segment forms part of the region that shows increasing helical character upon increasing concentration as observed by NMR (33). Next, to search for stable configurations populated in the two-chain ensemble, we computed a free energy surface quantifying the relative energetic favorability of different configurations binned as a function of the two order parameters selected to represent intermolecular assembly: the number of hydrogen bonds and number of hydrophobic contacts between the two protein chains (Fig. 1*C*). Two distinct minima (ΔG values < 10 kJ/mol relative to most populated reference bin), which we term strongly and weakly bound states, are observed. Averaging over only the configurations corresponding to the strongly bound free energy well (i.e., configurations in favorable intermolecular contact), we see a more significant increase in α-helical content in this 330–334 region (Fig. 1*B*) and stabilization (∼25% population) of a continuous helix spanning from residues 320–334, abruptly ending at residue G335 (Fig. 1*D*). Furthermore, the simulations suggest heterogeneity in the bound ensemble. Many different residue pairs in the region spanning 320–343 form intermolecular contacts (*SI Appendix*, Fig. S1*A*). The strongly bound ensemble also comprises heterogeneous binding orientations, including parallel and antiparallel helix–helix interactions, as well as interactions involving disordered conformations of the 320–343 region (*SI Appendix*, Fig. S1 *B* and *C*). Although two chains may not be sufficient to explore the full ensemble of bound configurations (i.e., TDP-43 may form trimeric or higher order helical assemblies), these data demonstrate how self-interaction can promote helical stabilization. Furthermore, these data are consistent with our previous NMR paramagnetic relaxation enhancement data, which suggested that the TDP-43 CTD 320–343 region visits multiple bound orientations (33).

Our previous work demonstrated that, even in the absence of phase separation, the CR of TDP-43 CTD self-assembles mediated by helix–helix contacts into a multimer state invisible to standard NMR approaches (33). To experimentally trap a dimer state, we mimicked the two-chain simulations by forming obligate CTD dimers in vitro by covalently cross-linking two CTDs far (>40 residues) from the conserved 320–343 region (Fig. 1*E*). We created two distinct disulfide cross-linked dimers, oxidized by copper (II) phenanthroline, at single cysteines engineered at residues 273 or 387 (Fig. 1*E*). After disulfide linkage, these CTD variants appear at twice the apparent molecular weight compared to reduced control samples in (nonreducing) SDS/PAGE (Fig. 1*F*). Consistent with stabilization of a structured assembly, fingerprint 2D (^{1}H–^{15}N transverse relaxation optimized spectroscopy [TROSY]) spectra of both S273C dimers (10 μM, in monomer units) and S387C dimers (20 μM) reveal shifted, very weak resonances. Nearly all of the resonances move "up" in the same direction toward lower ^{15}N chemical shift values ("up field"). This chemical shift perturbation is consistent with enhanced helicity as we previously observed upon increasing concentrations of non–cross-linked wild type (WT) (33), where we showed by ^{13}C-based experiments that shifts in this direction correspond to enhanced helicity. The identity of these resonances can be assigned to the 320–343 region by extrapolation of resonances of the WT TDP-43 CTD as a function of increasing concentration (i.e., increasing population of an assembled state) (Fig. 1*G*). In other words, we observe chemical shift perturbations for 12 distinct residue positions in both cross-linked dimers lying along the same vectors as observed for increasing concentrations of the non–cross-linked form. This similarity in chemical shift perturbation for cross-linked and non–cross-linked CTD strongly suggests that the cross-link does not bias the helix–helix contacts into a particular geometry (i.e., bias to form a parallel assembly due to symmetric cross-link site). Because each $^{1}H/^{15}N$ chemical shift position is a highly sensitive and an independent reporter of chemical environment (not simply helicity), changes in the underlying conformational ensemble due to the cross-link would instead result in a distinct pattern of chemical shifts. The lack of biasing of the structural ensemble of helix–helix interactions is reasonable due to the long (40-residue) region between the cross-link site and the helical region, resulting in an 80-residue distance between helical regions on linked dimers. Quantification of ^{15}N chemical shift differences between dimeric (oxidized) and monomeric (reduced) CTD revealed upfield chemical shifts from residues 315–343, primarily in 321–335, as well as at the site of the cross-link (Fig. 1*H*). Importantly, both cysteine variants display the same pattern of upfield shifts in the 321–340 region (rmsd ∼0.07 ppm), indicating that the chemical environment and hence the dimeric states sampled by the 321–340 region are independent of cross-link position. Furthermore, the magnitude of the ^{15}N chemical shift differences observed here is similar to those we derived for the assembled state of TDP-43 CTD based on experimental Carr–Purcell–Meiboom–Gill relaxation dispersion NMR experiments (33). Interestingly, these obligate dimer samples aggregated at higher concentrations, precluding more extensive NMR characterization. Taken together, the computer simulations and experiments show signatures of greatly enhanced helicity upon dimerization focused in the region from residue 321–335.

Mutations at Glycine Positions Enhance CTD α-Helical Structure in the 330–343 Region. As we find disruption of the TDP-43 CR helicity near G335 and G338, we wondered whether replacing G335 or G338 with other residues would increase helicity. To test the hypothesis that substitution of residues that are less helix-discouraging would enhance TDP-43 CTD helicity, we designed several TDP-43 CTD variants at G335 and G338 positions to observe the effect of these amino acids on TDP-43 CTD helicity. First, we conducted single-chain all-atom molecular dynamics simulations of the same 41-residue fragment, TDP-$43_{310–350}$, with

a set of single point mutations, changing G335 or G338 from glycine to the helix-promoting residue alanine (G335A and G338A). Mutating glycine to alanine (G335A and G338A) results in a significant increase of α-helical content in the simulations, particularly in the vicinity of the mutation sites (Fig. 2*A*). The increase in helical content is highest within residues 331–343 (Fig. 2 *B*, *Right*, and *SI Appendix*, Fig. S2 *A* and *B*), while helical content in residues in the preceding partially helical region 321–330 does not increase (Fig. 2 *B*, *Left*). G335D, an ALS-associated variant, has similarly enhanced helicity from 331 to 343, as do engineered variants G335N (similar to G335D but with the uncharged amide analogous residue) and G335S. This suggests that the removal of the unique backbone conformational flexibility of glycine, not specific contacts mediated by the sidechain, enhance helicity. Quantifying the helical enhancement, the maximum length of contiguous α-helical conformations (45) increases for G335A (i.e., helices spanning 320–337) and the population of longer helical conformations increases (Fig. 2*C*). For G338A, long helices are populated extending through position 338, which are not observed for WT. We note that the decrease in helicity in the

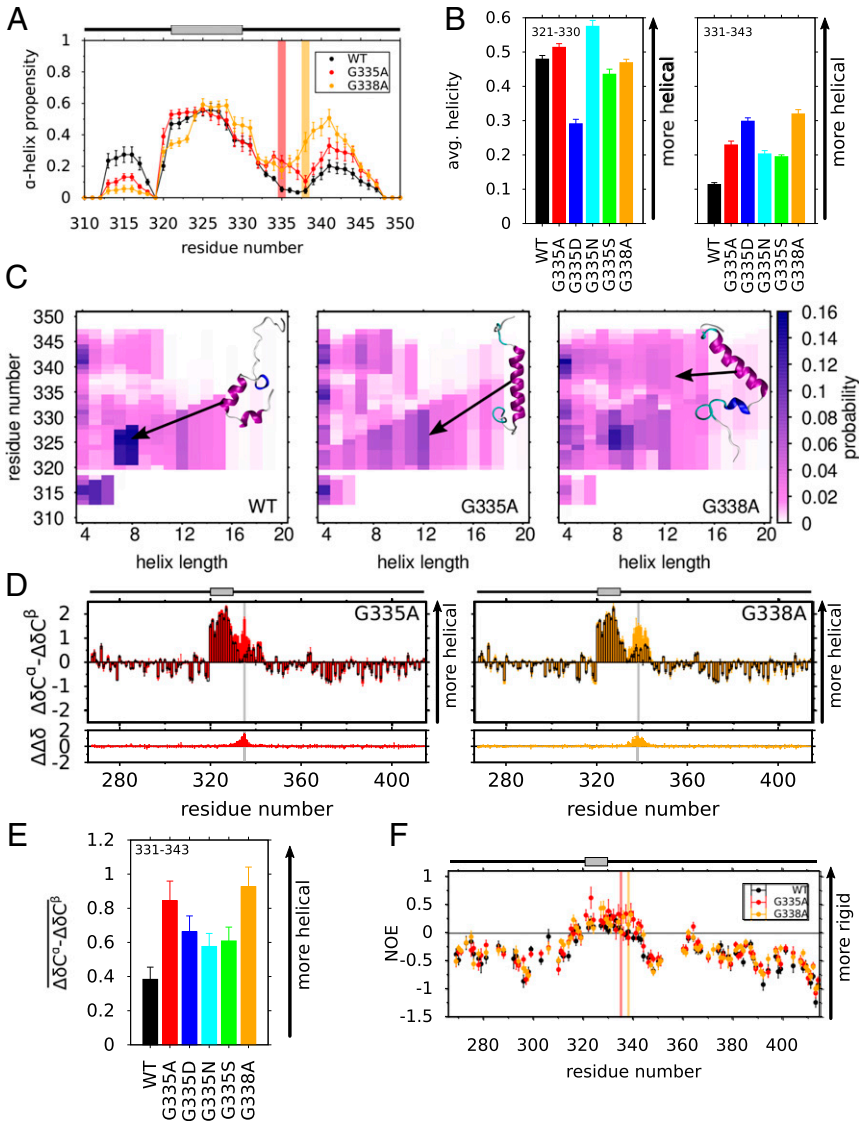

Fig. 2. G335 and G338 substitutions enhance TDP-43 CTD helical stability. (*A*) Per-residue α-helical propensities for WT, G335A, and G338A for atomistic single-chain simulations of TDP-43$_{310–350}$ show higher fraction of α-helical structure near the sites of mutation (highlighted by red, G335A, or orange, G338A, bars). Data are plotted as mean ± SEM of $n = 5$ equal divisions of the total dataset. (*B*) Average simulated helicity is mostly unaffected for residues 321–330 (*Left*) away from G335 and G338 mutation sites but enhanced for 331–343 (*Right*) surrounding the mutation site. (*C*) Maps of contiguous α-helical structure location (*y* axis) and length (*x* axis) for TDP-43$_{310–350}$ show increased probability for longer helix structure in G335A and G338A relative to WT. One example configuration from a subpopulation of the simulation ensemble (indicated by the black arrow) is displayed for each variant. (*D*) Experimental NMR secondary chemical shifts $(\Delta\delta C^{\alpha} - \Delta\delta C^{\beta})$ and the differences in secondary shifts with respect to WT (ΔΔδ) for G335A and G338A show increased α-helical structure near the site of mutation. The secondary shift values for WT are overlaid in black for comparison. (*E*) The average experimental secondary shift $(\Delta\delta C^{\alpha} - \Delta\delta C^{\beta})$ for TDP-43 331–343 of WT and mutant CTD highlight increases in local α-helical structure in all variants. Error bars are SEM. (*F*) Higher $\{^1H\}$–^{15}N heteronuclear nuclear Overhauser effect (NOE) values measured for G335A (red) and G338A (orange) compared to WT (black) near the site of mutation indicate slowed local protein backbone motion, consistent with enhanced helical structure. Mutation positions G335A and G338A highlighted with red and orange lines, respectively. For all above panels: Simulation data are plotted as mean and SEM from 10 equal blocks of equilibrated structural ensemble. Unless otherwise stated, experimental data are plotted as mean and SD estimated from signal-to-noise ratio.

region 313–318 far from the mutations for G335A and G338A simulations may be due to peptide end effects as we use a small TDP-43 CTD fragment in simulation to help converge the structural ensemble. The simulations show overall low (<25% for all variants) helicity in this region, and the experimental chemical shifts are consistent with low helicity in this region for all variants (see below).

With strong computational support for enhanced helicity of G335 and G338 point variants, we next characterized the secondary structure of TDP-43 CTD variants experimentally by comparing NMR chemical shifts of WT and mutant TDP-43 CTD variants. Positive values of the difference of the residual $^{13}C\alpha$ and $^{13}C\beta$ chemical shifts compared to a random coil reference database, $\Delta\delta C^{\alpha} - \Delta\delta C^{\beta}$ (Fig. 2*D*), indicate the presence of α-helical structure. Relative to WT, all of the G335 and G338 point mutants show positive increases in secondary shifts, ΔΔδ (Fig. 2*D* and *SI Appendix*, Fig. S2*C*), consistent with the enhanced helical content predicted by simulation. As suggested by the simulations, the pattern of local α-helical enhancement is distinct for G335A and G338A; enhancements are observed from 330 to 339 for G335A and 335 to 343 for G338A (Fig. 2*D*). Importantly, the values of $\Delta\delta C^{\alpha} - \Delta\delta C^{\beta}$ near the site of mutation nearly reach the level seen in the 321–330 region, which is ∼50% helical (33). To compare the helical enhancement between all variants, we computed the average secondary shift across residues 331–343, $\overline{(\Delta\delta C^{\alpha} - \Delta\delta C^{\beta})}$ (Fig. 2*E*). Average secondary shift values for residues 331–343 of WT and mutant CTD are strongly correlated ($r = -0.972$) with the predicted change in free energy of helix stabilization relative to glycine (46) (*SI Appendix*, Fig. S2*D*). To further probe for enhanced helical structure in TDP-43 CTD, we measured NMR relaxation parameters sensitive to reorientational motion at each position, which is slower for structured conformations than for disordered conformations. Heteronuclear nuclear Overhauser effect values, $\{^1H\}$–^{15}N NOE, for G335A and G338A are slightly higher than WT in the region from 330 to 343 (Fig. 2*F*), consistent with a higher population of structured, slow-moving conformations. We conclude this because heteronuclear NOE values increase as HN bond vector reorientation slows and, at 500 MHz ^1H Larmor frequency, are sensitive to reorientational motions in the range of timescales from 0.1 to 3 ns (47). Changes in motions outside these timescales are not captured in this measure. Similarly, higher values of the transverse relaxation rate constant, ^{15}N R_2, are associated with slower reorientational motions (47) and are observed for G335A and G338A. To ensure that the observation of higher ^{15}N R_2 is not due to chemical exchange effects arising from transient helix–helix contact formation (*SI Appendix*, Fig. S2*E*; see below), we also measured the cross-correlated relaxation rate, η_{xy}, which is independent of these exchange effects. Like the $\{^1H\}$–^{15}N NOE, η_{xy} is enhanced from 331 to 343 in G335A and G338A, consistent with slower motion in the 331–343 region. Differences in ^{15}N spin relaxation parameters for WT, G335A, and G338A are negligible across the remainder of the CTD, suggesting that the variants do not change the overall folding of the monomeric CTD (e.g., they do not promote the formation of new tertiary structure such as intramolecular helix bundling). Taken together, these data strongly suggest that single point variants at conserved glycine positions in TDP-43 331–343 enhance TDP-43 CTD helicity with a magnitude commensurate with their predicted ability to stabilize the α-helix structure.

G335 and G338 Mutations Enhance Intermolecular Helix–Helix Contacts and Higher-Order Assembly. In our previous work, we showed that ALS-associated variants Q331K, M337V, A321G, and A321V disrupt the intermolecular helix–helix assembly of TDP-43 CTD (33). Here, we wondered whether TDP-43 CTD variants that enhance helicity in 331–343 region increase TDP-43 CTD assembly. For this purpose, we used the same approach, measuring the concentration-dependent perturbations of NMR resonances in fingerprint (^1H–^{15}N heteronuclear single-quantum coherence [HSQC]) spectra for G335 and G338 variants at concentrations ranging from 10 to 90 μM at conditions where phase separation does not occur (i.e., 0 mM NaCl). We then calculated chemical shift perturbation (Δδ) at each concentration relative to a monomeric reference for each variant (i.e., the concentration below which we do not detect significant chemical shift differences = 20 μM for all variants except for G338A = 10 μM; Fig. 3*A*). As shown previously (33), WT CTD displays upfield ^{15}N Δδ in the 321–340 region above 20 μM, indicative of local intermolecular interactions. G335A and G338A show ^{15}N Δδ at the same residue positions as WT but are significantly enhanced at 30 μM compared to WT. Above 30 μM, many of the resonances in G335A and G338A are broadened beyond detection (Fig. 3*A*), consistent with enhanced intermolecular interactions, compared to WT, which shows resonance loss due to broadening only above 90 μM.

To quantify the effects of G335 and G338 variants on intermolecular self-assembly in the 321–343 region, we used linear regression to normalize the relative magnitude of ^{15}N chemical shift perturbations at all residue positions, Δδ, for WT and mutant CTD variants at each concentration to the same standard for all variants, which we termed CSP_{norm} (Fig. 3*B*). As a standard, we use the difference in ^{15}N chemicals shifts observed at all residue positions for WT at 45 μM (partially assembled) and at 20 μM (monomeric sample). CSP_{norm} is higher for all G335 and G338 variants relative to WT, suggesting that these mutations enhance intermolecular interactions in the 321–343 region. G338A displays the largest increase in CSP_{norm} values followed by G335A and G335D, and weaker enhancements caused by G335S and G335N. As we previously observed for WT (33), CSP_{norm} values for all variants increase approximately linearly as a function of increasing CTD concentration, suggesting that the population of the assembled state is not saturated at these concentrations. Importantly, the enhancement of helix–helix assembly due to each variant follows the same order as the enhancement in helicity of the monomeric CTD; the only exception is G335D, whose lower net charge likely favors assembly in these low salt conditions (48). Together, these observations suggest that higher helicity of TDP-43 CTD monomer enhances the helix–helix assembly by increasing the effective affinity.

High concentration samples that contain significant populations of the assembled form, however, show significant line broadening in the region of the helix for all variants, precluding our ability to probe saturation of binding and to determine the dissociation constant for assembly. Instead, we took advantage of the remaining resonances far from the assembly site and still visible at high concentrations to probe the average hydrodynamic size as a function of concentration. To this end, we measured translational diffusion coefficients for WT CTD at sample concentrations ranging from 10 to 600 μM. Intensity ratios for all concentrations decay as a single exponential as a function of squared gradient strength (*SI Appendix*, Fig. S3), suggesting that the translational diffusion of the CTD at each concentration can be best captured by a single diffusion coefficient (D), reflecting the population-weighted average diffusion rates for monomeric and oligomeric states consistent with dynamic, reversible assembly (49). At low CTD concentrations (50 μM and below), the apparent diffusion coefficient for WT CTD remains mostly unchanged ($8.8 \pm 0.1 \times 10^{-11}$ $m^2 \cdot s^{-1}$) (Fig. 3*C*), suggesting that this value reflects the diffusion coefficient of monomeric CTD. This diffusion coefficient corresponds to an approximate radius of gyration of 2.8 nm in dilute aqueous solution, close to that of the similar-length low-complexity (LC) domain of hnRNPA2 (50) and significantly more extended than the globular reference protein lysozyme (2.03 nm) (*SI Appendix*, Fig. S3*A*), which is of almost

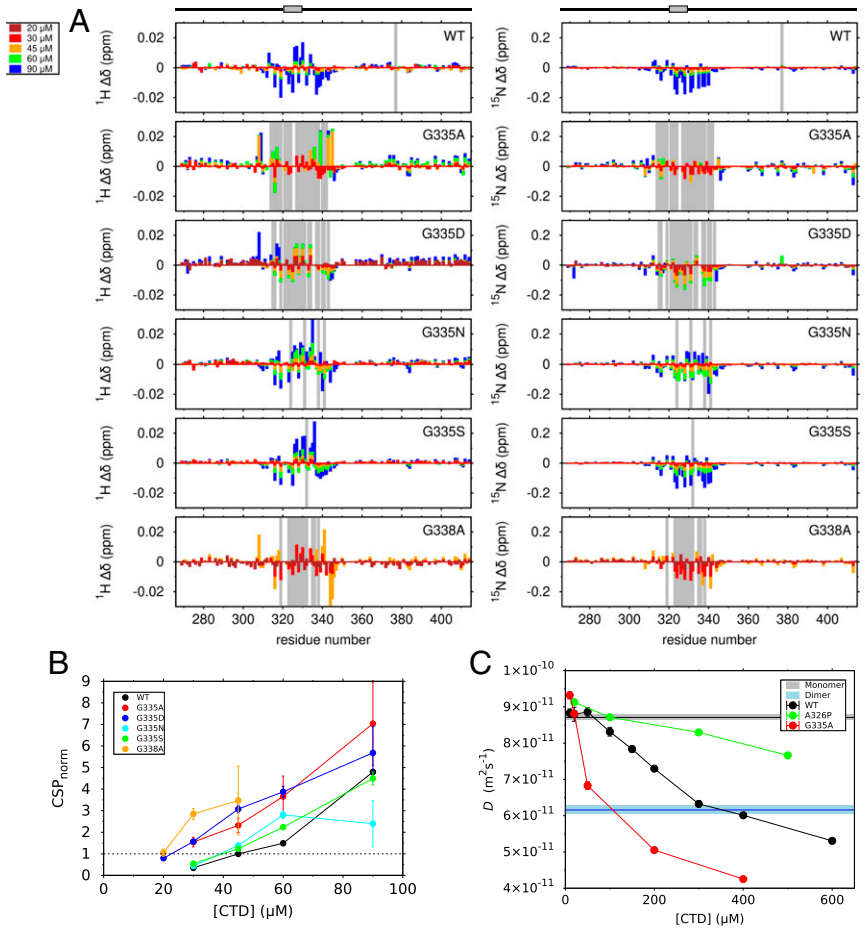

Fig. 3. Mutations enhance TDP-43 CTD helix–helix interaction and assembly. (*A*) Larger chemical shift differences (Δδ) in the helical region of TDP-43 CTD for G335A and G338A compared to WT are consistent with enhanced helix–helix interactions. Shifts are reported at concentrations from 20 to 90 μM with respect to a monomeric (low concentration) reference (20 μM for WT and G335A; 10 μM for G338A). The gray boxes indicate the loss of detectable peak intensity due to line broadening. (*B*) Normalized chemical shift differences vs. concentration are higher for mutant CTD compared to WT, consistent with increased self-assembly for G335 and G338 variants. Error bars are SD estimated by 100 bootstrapping simulations derived from experimental uncertainty. (*C*) Diffusion coefficients calculated from NMR diffusion data plotted as a function of CTD concentration show that WT (black) and G335A (red) diffuse slower than A326P (green). Average diffusion coefficients for S273C and S387C dimers and S273C and S387C monomers are indicated by blue and black horizontal lines, respectively. Data are plotted as mean ± SD, indicated for monomer and dimer diffusion coefficients by gray and light blue boxes, respectively.

identical molecular weight to TDP-43 CTD. At concentrations above 50 μM, however, the apparent diffusion coefficient of the CTD sample decreases, consistent with dynamic assembly of CTD into higher-order species in rapid equilibrium with the monomeric state, consistent with our NMR-based model of CTD assembly (33). We note that if slow- or nonexchanging species were significantly populated, one would expect to see nonexponential behavior in the diffusion curves (49). We do not observe such nonexponential behavior as diffusion data were extracted by fitting to a single diffusion time, and the fits are good (*SI Appendix*, Fig. S3). These diffusion data alone, however, do not uniquely determine the oligomerization state. To provide a reference for the diffusion of a TDP-43 dimer, we also measured the translational diffusion coefficients of the monomeric and covalent dimeric forms of the S273C and S387C CTD variants at low (5 μM) concentrations (Fig. 3*C* and *SI Appendix*, Fig. S3*B*). Diffusion coefficients are similar for both cross-linked dimers. The diffusion coefficient for reduced monomeric CTD ($8.7 \pm 0.1 \times 10^{-11}$ m^2·s^{-1}) is effectively the same as the WT, whereas the covalent dimer has a smaller diffusion coefficient ($6.4 \pm 0.1 \times 10^{-11}$ m^2·s^{-1}). The diffusion coefficient at high concentrations is also smaller than that of the covalently linked dimer, suggesting that oligomers larger than dimers are present. For the G335A variant, oligomerization occurs at a much lower concentration. Hence, G335A self-associates at lower concentrations compared to WT, implying tighter binding than WT. To demonstrate that higher-order structures, not increased nonspecific contacts or increased viscosity due to increased protein concentration, give rise to the slower diffusion coefficients observed, we tracked the diffusion as a function of concentration of the helix-disrupting A326P variant (33) that does not assemble (Fig. 3*C*). This variant shows only modestly slower diffusion even at high concentration, suggesting that the sharply decreasing diffusion coefficient as a function of concentration observed for WT and G335A arises due to assembly in the concentration range tested. Taken together, these data suggest TDP-43 CTD assembles into states larger than dimers and that such an assembly happens at lower concentrations for the interaction-enhancing G335A variant.

G335 and G338 Variants Alter In Vitro LLPS. Given the relationship between TDP-43 CTD intermolecular self-assembly and LLPS, we next tested whether the G335 and G338 variants that increase interaction also enhance phase separation. Although the CR mediates helix–helix contacts at all conditions, TDP-43 CTD does not readily phase separate in the absence of salt, which appears to induce or enhance interaction between the polar-residue regions of TDP-43 as well as other prion-like domain proteins (33, 50, 51). To monitor the effect of G335 and G338 variants on phase separation, we mapped the low concentration arm of the phase diagrams as a function of increasing NaCl using a recently developed approach (7, 50, 52). In our case, LLPS was initiated by a brief incubation of 20 μM CTD with a given concentration of NaCl, followed by centrifugation to sediment the micrometer-sized droplets making up the phase-separated state (i.e., the protein-dense phase). We then measured the concentration of protein in the supernatant (i.e., the protein-dispersed phase). The amount of TDP-43 CTD remaining in the supernatant decreases for WT CTD as a function of NaCl concentration, suggesting CTD is undergoing LLPS (Fig. 4*A*) with "salting-out" behavior, similar to our previous work on TDP-43 CTD (33) as well as FUS LC (51) and hnRNPA2 LC (50). In the cases where LLPS is observed, the concentration remaining in the supernatant can be equated to the saturation concentration

(C_{sat}) (i.e., the concentration of CTD above which LLPS will occur at these conditions). Ideally, one would also like to measure the dense phase protein concentration to complete the phase diagram, but TDP-43 CTD droplets convert to aggregates over the timescale of forming a large enough droplet to isolate (33). Both the ALS-associated variant Q331K as well as the LLPS-disrupting engineered variant M337P display higher remaining protein in the supernatant than WT for any given salt concentration, consistent with our previous findings that these mutations discourage CTD assembly and phase separation (Fig. 4*A*) (33). Conversely, G335 and G338 variants all show a lower concentration of protein remaining in the supernatant compared to WT, suggesting that these single point variants are significantly more prone to phase separate. Micrographs of the mutant CTD after phase separation show no morphological differences of these variants compared to WT and no evidence of increased protein aggregation (Fig. 4*B*), suggesting that changes in protein remaining in the supernatant faithfully report on TDP-43 CTD LLPS and not on a transition to aggregation in these conditions. Of our engineered CTD variants, G335A and G338A show the greatest enhancement of LLPS, with only about 5 μM remaining in the supernatant at 150 mM NaCl (i.e., physiological ionic strength) conditions, a nearly three times decrease compared to WT (~15 μM). The G335D, G335N, and G335S variants displayed more modest enhancements, with ~10 μM remaining. Thus, single substitutions can dramatically enhance phase separation via enhancement of helix–helix contacts. Importantly, these saturation concentrations for TDP-43 CTD variants show a strong correlation with changes in CTD secondary structure (Fig. 4*C*) more so than with amino acid hydropathy (53) (*SI Appendix*, Fig. S4 *A* and *B*), suggesting that α-helical structure stabilized by the amino acid at that position, and not hydrophobicity change, accounts for the large changes in LLPS. Interestingly, only G335D shows a slightly different rank order in this saturation concentration as a function of increasing salt concentration. At low salt concentrations (<150 mM NaCl), the saturation concentration for G335D is lower (i.e., greater propensity to phase separate) than that of WT, G335N, and G335S, while at the highest salt concentrations tested (300 to 500 mM NaCl), it is approximately the same as WT and is higher (less prone to phase separate) than G335N and G335S. This change as a function of salt may arise because G335D decreases the net charge of TDP-43 CTD, leading to less long-range repulsion at low salt conditions lacking salt to screen these effects (48). In total, however, the correlation between extent of phase separation and helicity is strong at all salt concentrations (*SI Appendix*, Fig. S4*C*), suggesting that helicity is the dominant factor in determining phase separation of all variants including G335D.

To further elucidate the potential contributions of hydrophobicity vs. helicity to TDP-43 phase separation, we conducted coarse-grained simulations of TDP-43 CTD coexistence following the simulation model and framework from our previous work (54–56). Because this coarse-grained model treats protein chains as flexible polymers and secondary structure is not directly captured, these simulations decouple the mutational change in hydrophobicity from the changes in helicity, which are inseparable in the experiment and traditional all-atom molecular simulation. Even in the absence of helicity in the CR, self-interaction at the 310–340 region is slightly favored, as seen by elevated contact probability in coarse-grained simulations of the condensed phase (*SI Appendix*, Fig. S4*D*). Changing only the amino acid sequence in the coarse-grained model (e.g., G335A) and hence the favorability of interactions, there is no appreciable change in the phase diagram (Fig. 4*D*). We then tested the effects of the α-helical configuration by using rigid-body constraints to effectively force the subregion identified by two-chain all-atom simulation (residues 320–334; Fig. 1*B*) into an α-helical configuration (Fig. 4*E*). When we compare the results from fixed-helix coexistence simulations (Fig. 4*F*) and those using fully flexible chains, we see that the phase diagram shifts upward to higher temperatures (Fig. 4*E*), indicating a greater phase separation propensity for the fixed-helix chains. Upon the introduction of α-helices, the saturation concentration, indicated by the left arm of the coexistence curve, decreases by roughly a factor of 2 across a broad range of temperatures tested (Fig. 4 *E*, *Inset*). These results provide direct evidence that the presence of short α-helical structure can promote self-interaction and hence enhance phase separation of TDP-43 CTD, more so than just the increase of side-chain interaction strength.

G335 and G338 Variants Affect In-Cell LLPS Fluidity and Splicing Function. To elucidate how changes in CR helicity impact TDP-43 phase behavior and function in a cellular context, we tested the G335 and G338 point mutations in the context of established cell-based reporter assays for TDP-43 phase dynamics and splicing function. We first introduced G335 and G338 mutations into the TDP-$43_{RRM\text{-}GFP}$ construct, previously developed to determine the effect of single point mutations on TDP-43 phase fluidity in cells. In these cells, the vast majority of the expressed TDP-$43_{RRM\text{-}GFP}$ partitions into a single, large nuclear TDP-43 reporter droplet phase formed in each cell nucleus, and the fluidity of this TDP-43 phase is monitored by fluorescence recovery after photobleaching (FRAP) (35). Here, we measured fluorescence signal recovery for WT and mutant droplets over time (Fig. 5 *A*–*D*). For comparison, we included only droplets of similar size and signal levels in our analysis. Previously tested CTD variants that disrupt helix–helix interaction show increased fluidity due to decreased intermolecular interaction, while removal of the conserved segment prevented phase separation (35). Here, we now show that CTD mutants G335N, G335S, and G335A instead display decreased droplet fluidity relative to WT (Fig. 5 *B* and *D*). G335A shows the greatest reduction of fluidity, while G335N and G335S show intermediate droplet fluidity. Importantly, the rank order of the in-cell fluidity matches that of the in vitro C_{sat} at 150 mM NaCl (see Fig. 4) (except for G335D; see below), although some observations were unexpected, highlighting the importance of the cellular context. In particular, FRAP profiles were variable among G335S droplets for reasons not clear at this point (*SI Appendix*, Fig. S5*A*), and the magnitude of the difference in fluidity between G335S and G335N is not predicted from the in vitro ranking. Regarding the disease-associated variant G335D, the in-cell FRAP recovery time of G335D droplets is not significantly different from that of WT (Fig. 5 *A* and *B*), similar to the in vitro LLPS at high salt. Taken together, these findings show that increasing CR helix propensity by mutating G335 and G338 not only lowers C_{sat} for phase separation in vitro but also reduces TDP-43 fluidity in a tunable manner correlated with the properties observed in vitro. Our data furthermore suggest that C_{sat} and droplet material properties can be precisely tuned by single amino acid changes in the helix–helix interacting region.

Considering the links between TDP-43 assembly and splicing function (21, 36), we next sought to investigate whether mutations at G335 and G338 can alter its ability to facilitate exon skipping in the cystic fibrosis transmembrane conductance regulator (CFTR) minigene splicing assay (57). Previously, it was shown that deletion of the CR containing the helix in TDP-43 CTD disrupted RNA splicing (40). Here, we wanted to test whether enhanced TDP-43 CTD helicity and helix–helix interaction not only promote phase separation but also alter splicing function. To this end, we performed rescue experiments in TDP-43 knockdown HeLa cells comparing the regulation of CFTR exon 9 splicing by mutant and WT TDP-43. We measured the extent of exon skipping in small interfering RNA (siRNA)-treated cells expressing control, siRNA-resistant WT, G335, or G338 mutants (Fig. 5*E* and *SI Appendix*, Fig. S5*B*). The percentage of exon exclusion was normalized to WT to calculate the relative splicing regulatory activity for each mutant (Fig. 5*F* and

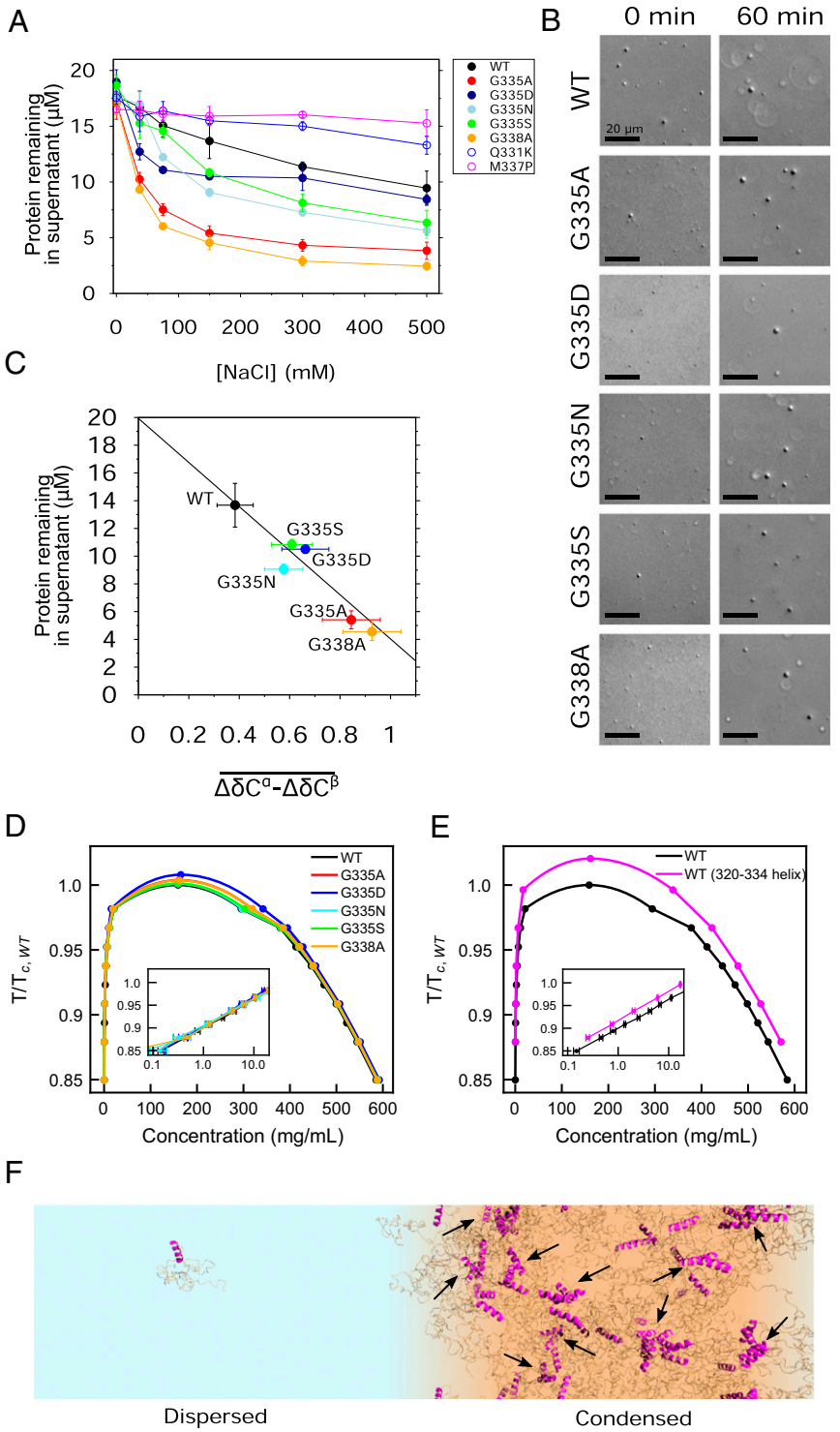

Fig. 4. Mutations at G335 and G338 alter in vitro LLPS. (*A*) Protein remaining in supernatant after phase separation for WT and mutant CTD measured for 0 to 500 mM NaCl. Error bars represent SD of three replicates. (*B*) DIC micrographs of LLPS for WT TDP-43 CTD and variants G335A, G335D, G335N, G335S, and G338A at 0 and 60 min after addition of NaCl to 300 mM. (Scale bars, 20 μm.) (*C*) The protein concentration remaining in supernatant of WT and mutant CTD at 150 mM NaCl ("physiological conditions") correlates well with the average change in secondary shift $(\overline{\Delta\delta})$ (Pearson $r = -0.95$). Error bars represent SD of concentrations using three replicates and SEM for $\Delta\delta C^{\alpha} - \Delta\delta C^{\beta}$. (*D*) Coexistence curves of TDP-43 CTD from coarse-grained (CG) slab simulations of WT and G335/G338 mutants illustrate no discernable difference in LLPS behavior as a result of mutation. The *Inset* shows the low-concentration phase on a log scale and highlights the similarity even at very low concentrations. (*E*) Coexistence curves of TDP-43 from CG slab simulations illustrate enhanced phase separation when residues 320–334 are fixed as a rigid helix (magenta) instead of fully flexible (black). *Inset* shows the approximately twofold change to left arm of the phase diagram with temperature vs. concentration on a log scale. (*F*) A snapshot of the TDP-43 CTD CG slab simulation where CTD molecules harboring rigid α-helical substructure (magenta) visit both dispersed and condensed states in phase coexistence. Arrows indicate oligomers formed by helix–helix contacts.

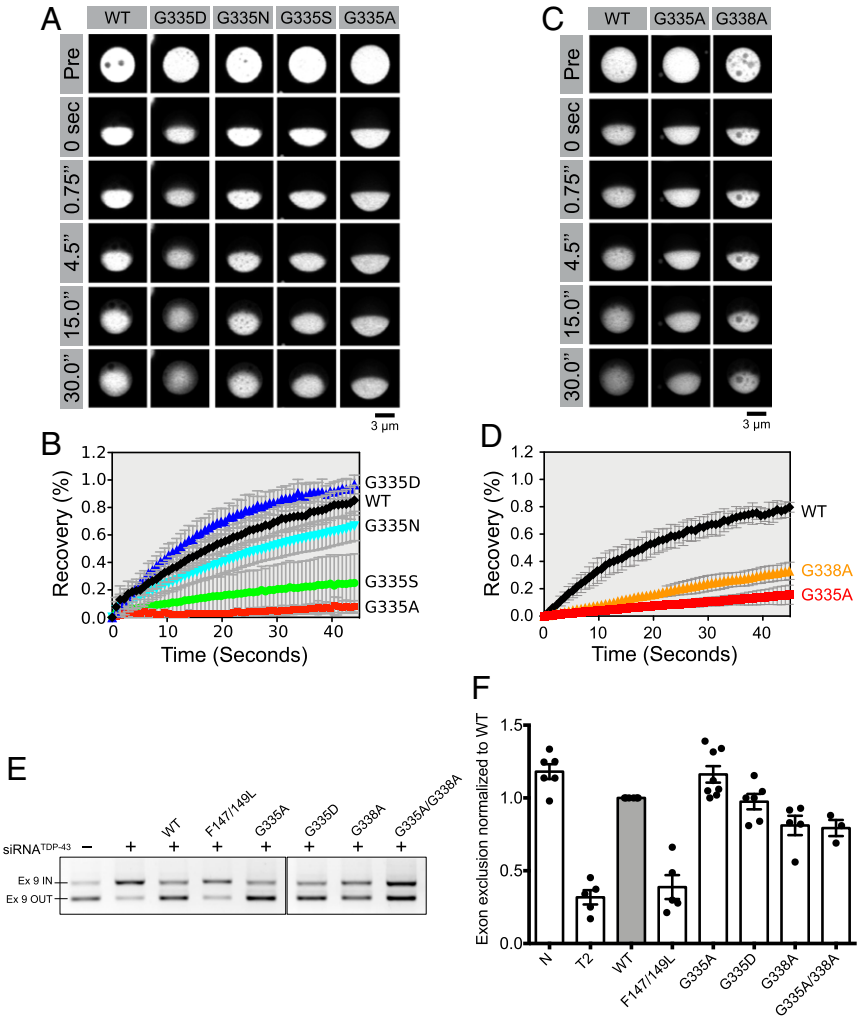

Fig. 5. Mutations at G335 and G338 alter in-cell LLPS fluidity and splicing function. (*A*–*D*) Fluorescence recovery after in-cell half-droplet photobleaching and quantification for TDP-43$_{RRM-GFP}$ reporter construct with (*A* and *B*) WT, G335D, G335N, G335S, and G335A, or (*C* and *D*) WT, G335A, and G338A CTD sequences. TDP-43$_{RRM-GFP}$ shows differential droplet fluidity for G335 variants relative to WT. (*E*) Example agarose gel of PCR products to quantify the fraction of exon 9 CFTR exclusion (OUT) expressed from a minigene construct transfected in HeLa cells. Cells were treated with control, TDP-43 siRNA, or TDP-43 siRNA plus WT or mutant vectors. (*F*) The splicing activity was calculated as the ratio of exon 9 exclusion in HeLa cells expressing siRNA-resistant WT and mutant constructs (as labeled) or in absence of exogenous TDP-43 expression (T2). Nonspecific siRNA was used as control (N). Error bars are SEM of three or more replicates.

SI Appendix, Fig. S5*C*). As a negative control, we included the RNA-binding deficient variant F147L/F149L in our assays. Importantly, the G335A variant shows increased activity compared to WT ($P < 0.004$), suggesting that a single point substitution can indeed enhance the TDP-43 function. Contrary to our expectations and unlike the enhancement observed for G335A, G335D and G338A show slightly decreased splicing activity compared to WT. This difference between G335A and G338A in splicing effect may be due to differential alterations in interactions with binding partners, including hnRNPA2 mediated via the CR of TDP-43 CTD that contributes to TDP-43 splicing activity (40) or by nonnatural overstabilization of the TDP-43 interaction. Indeed, in cellular stress conditions, G338A (and G335A) appear to increase cytoplasmic mislocalization and aggregation of full-length TDP-43 compared to WT (*SI Appendix*, Fig. S5*D*). Thus, even though phase separation and splicing activity can be increased in cells by point mutations in the CR, TDP-43 self-interaction, droplet fluidity, and splicing function may be precisely balanced by sequence to prevent aggregation and preserve robust physiological function across differing cellular conditions.

Discussion

Diverse structural elements spanning the spectrum from completely disordered regions to globular domains have been shown to contribute to the interactions that undergird biomolecular LLPS. The role of the CR within TDP-43 CTD comes into focus here. We show that the α-helical structure of the region can be increased in direct proportion to the α-helix stabilizing propensity of the amino acid substituted at a glycine position, with the helix-promoting alanine substitution having the greatest effect. These data suggest that the backbone conformational entropy discourages helix formation in the 331–343 region of TDP-43, as substitution of glycine 335 with any of several small amino acids (including G335A, G335S, G335N, and G335D) all enhanced the helical structure. This helix stabilization, in turn, enhances TDP-43 CTD helix–helix interaction and phase separation. These data complement our previous report that variants in the same subsection of the CR spanning residues 331–343 that becomes helical only upon helix–helix assembly (M337V ALS-associated mutation and the helix-disrupting M337P engineered variant) both discourage helix–helix assembly and phase separation (33). Given that the helix-stabilizing variants enhance interactions and phase separation, reducing backbone conformational entropy via substitutions at glycine residues in TDP-43 CTD CR appears to stabilize protein interactions at this site. We note that the G335D ALS-associated variant increases helicity and helix–helix interaction in low salt conditions, although phase separation in vitro and in cell as well as splicing function are similar to WT. Hence, the precise cause of disease for this mutation that alters the conserved helix-forming region is not clear.

Importantly, the TDP-43 helical region appears unique among RNA-binding proteins—homologous (i.e., evolutionarily related) hydrophobic-residue–rich sequences are apparently not found in other related human proteins. This hydrophobic region seems

out of place amid the polar (e.g., FUS, hnRNPA2, remainder of TDP-43 CTD) or highly charged (e.g., ddx4) (3) low-complexity sequences known to mediate LLPS. However, other phase-separating proteins such as TIA-1 contain predominantly disordered domains with conserved helix-inducing residues (especially alanine, which is enriched in the TDP-43 CR), suggesting that TDP-43 CTD may be one in a class of natural proteins containing helical modules that form upon and contribute to phase separation. Importantly, unlike traditional coiled-coil or leucine zipper helix–helix interactions (58), TDP-43 CTD CR encodes weak (K_d ~100 μM range) and dynamical helical interactions. This range of affinity is consistent with the multivalent but individually weak contacts formed within membraneless organelles and their dynamic, liquid nature where a tight contact (nanomolar range) with slow off-rate could inhibit responsive reorganization of the functional complexes. Indeed, the apparent interaction strength is commensurate with self-assembly domains already characterized in the remainder of TDP-43: the polar-rich prion-like majority of the CTD that assembles via individually weak multivalent contacts (33), and TDP-43 N-terminal domain that forms weak (K_d ~100 μM) globular protein chains also enhancing phase separation (21). Similarly, the contacts formed by TDP-43 CTD CR are also heterogeneous (33), unlike amphiphilic α-helices that form ordered, rigid bundles. Indeed, CTD assembly may underlie the ability of this region of TDP-43 to interact with splicing factor partners, including hnRNPA2 (35, 40). Hence TDP-43 CTD CR serves as a dynamic and heterogeneous binding module to enhance TDP-43 self-interaction and phase separation.

The identification of single, specific sites that can be used to alter the assembly and material properties of cellular droplets substantially offers an important opportunity to use TDP-43 CTD as a module to tune phase separation in engineered fusion proteins. The multivalent interactions leading to phase separation lend themselves to modulation (59), and the TDP-43 CTD CR is shown here to be a uniquely short and tunable module. Interaction can be finely adjusted by single amino acid position changes to dramatically enhance or, as in our previous work, decrease interaction at this site (Fig. 3). Enhanced interactions of this region, in turn, increase phase separation both in vitro (Fig. 4) and in cells (Fig. 5), leading to enhanced function in cells. Therefore, TDP-43 CTD helical region serves as a small structural element that can be used to perturb or control phase separation. Furthermore, compared with repetitive low-complexity sequences (e.g., prion-like regions or arginine rich regions) (17) or globular protein/linear interaction motif pairs (e.g., SH3:proline-rich) (20), TDP-43 CTD's short (~20-residue) module functions with a fine ability to precisely tune phase separation to the desired degree, using the "knob" of mutations that can precisely increase or decrease interaction. Indeed, just as G335A can enhance helix–helix assembly and splicing function of native TDP-43, variants of the TDP-43 CR could be fused to/within other proteins to regulate their cellular functions within membraneless organelles. Furthermore, just as phase separation of low-complexity regions can be controlled by posttranslational modification (54), targeting modifications to sites adjacent to or within a TDP-43 helical module could be used to alter phase separation and function responsively. Therefore, a series of TDP-43 CTD variants could make for an important tool for engineering phase separation or, more broadly, for tuning dynamic self-organization.

Methods

Protein Expression and Purification. Point mutations were introduced into the TDP-$43_{267–414}$ (CTD) construct previously described (33) using QuikChange mutagenesis or overlap extension PCR with mutagenic primers (60).

WT and mutant CTD constructs were expressed in *Escherichia coli* BL21 Star DE3 (Invitrogen) cells in either LB media or, where indicated as uniformly labeled ^{15}N or $^{15}N/^{13}C$, in M9 minimal media supplemented with $^{15}NH_4Cl$ and/or ^{13}C-glucose as the sole nitrogen and carbon sources, respectively. Recombinant proteins were purified as previously described (33), with the exception that the TEV cleavage buffer was substituted with 20 mM Tris, 500 mM GndHCl, pH 8.0, for more efficient cleavage of the purification tag. Additionally, proteins were exchanged into Storage Buffer (20 mM Tris, 8 M urea, pH 8.0) before flash freezing and storage at −80 °C. For all experiments, purified proteins were desalted into MES Buffer (20 mM MES, pH 6.1) using 0.5 mL of Zeba spin desalting columns (Thermo Scientific) in accordance with manufacturer instructions.

NMR Spectroscopy. All NMR experiments were performed in 20 mM MES Buffer, pH 6.1 (pH adjusted with NaOH), supplemented with 10% D_2O. Experiments were recorded on Bruker Avance spectrometers operating at either 850- or 500-MHz ^1H Larmor frequency with TCI z-gradient cryoprobes at 25 °C. Backbone resonance assignments for CTD variants were obtained by standard triple-resonance experiments HNCACB and CBCACONH, as previously described (33). Subsequent secondary chemical shifts were obtained from comparison of experimental C^α and C^β chemical shifts with their respective predicted random coil reference chemical shifts (61, 62).

^{15}N R_1, ^{15}N R_2, and $\{^1H\}$–^{15}N heteronuclear NOE experiments were measured for 20 μM WT, 20 μM G335A, and 10 to 20 μM G338A ^{15}N-labeled CTD at 500-MHz ^1H Larmor frequency using standard pulse sequences (hsqct1etf3gpsitc3d, hsqct2etf3gpsitc3d, hsqc-noef3gpsi). Each ^{15}N R_1 experiment comprises seven interleaved ^{15}N R_1 relaxation delays: 100, 200, 300, 400, 600, 800, and 1,000 ms with a recycle delay of 1.5 s. Each ^{15}N R_2 experiment comprises six interleaved ^{15}N R_2 relaxation delays with a B_1 field of 556 Hz: 16.4, 32.8, 65.5, 131.2, 229.6, and 262.4 ms with a recycle delay of 2 s. $\{^1H\}$–^{15}N heteronuclear NOE experiments comprise interleaved proton saturation sequences and reference sequences without proton saturation with a recycle delay of 5 s. Measurement of η_{xy} was accomplished using the pulse sequence described previously (63), with a relaxation delay (T) of 42 ms and recycle delay of 1.5 s.

Chemical shift perturbations were quantified for either WT and mutant CTD variants by measuring the chemical shifts of ^1H–^{15}N cross-peaks of HSQCs acquired at 850-MHz ^1H Larmor frequency at concentrations ranging from 10 to 90 μM as previously described (33).

Pulsed-field gradient diffusion measurements for WT and mutant CTD at concentrations ranging from 10 to 600 μM acquired using the longitudinal eddy current delay with bipolar gradient scheme (64) provided in the Bruker standard library (ledbpgppr2), with 16 gradient strengths: 0.96, 5.39, 9.92, 13.62, 16.58, 20.10, 23.75, 27.26, 30.83, 34.37, 37.90, 41.38, 44.82, 48.08, 51.33, and 54.46 G/cm. The diffusion time was set to 250 ms with encoding/decoding gradient pulse lengths of 1 ms, using a recycle delay of 2 s. Gradient powers were calibrated based on the known diffusion coefficient of trace H_2O in a 99.8% D_2O sample (65). In all cases, intensity ratios were calculated by least-squares regression of select ^1H spectral regions for each gradient power against those of a reference gradient power (0.96 G/cm). SE of the intensity ratios was estimated with 100 bootstrapping simulations.

All NMR spectra were processed with NMRPipe (66) and analyzed with NMRFAM-Sparky (67). ^{15}N R_1, ^{15}N R_2, $\{^1H\}$–^{15}N NOE, and η_{xy} values and their respective SEs were calculated using in-house scripts.

Estimating R_{ex} for WT and G335A CTD. Chemical exchange contributions to ^{15}N R_2 (R_{ex}) were calculated based on the relationship:

$$R_2 = \kappa\eta_{xy}, \quad [1]$$

where κ is a scaling parameter that can be approximated for all residues as the trimmed mean of R_2/η_{xy} (68). In our case, two values of κ were calculated due to the differential relaxation rates across the CTD resulting from both structured and disordered regions. η_{xy} rates were first separated into one of two equal-width bins, and their respective κ values were obtained by solving Eq. **1**. Site-specific R_{ex} values were then calculated from R_2, κ, and η_{xy}, as follows:

$$R_{ex} = R_2 - \kappa\eta_{xy}. \quad [2]$$

Cross-Linking. CTD variants harboring engineered cysteine residues at one of two serine positions (S273C or S387C) were buffer exchanged and diluted to 100 μM in Storage Buffer (see above, which includes 8 M urea to maintain solubility). Cross-linking was initiated by addition of copper (II) phenanthroline (69) to a final concentration of 1 mM, followed by incubation at room temperature for at least 1 h. Reactions were quenched by addition of EDTA to 5 mM, and the resulting mixture was purified by size-exclusion chromatography with a 26/600 Superdex 75 equilibrated in Storage Buffer supplemented with 1 mM EDTA. Fractions corresponding to dimeric CTD were pooled, concentrated up to 750 μM ([dimer]), flash frozen, and stored at −80 °C. NMR samples were prepared by diluting 12.5 μL of the dimeric stock into 437.5 μL of MES Buffer, resulting in a final urea concentration of 200 mM. Samples were then centrifuged for 10 min at 12,000 rpm, and the concentration of the supernatant was measured by A_{280}. The samples were then diluted to the final desired protein concentration with 1:35 Storage Buffer:MES Buffer, thus ensuring the urea concentration remains constant.

In order to prepare monomeric control samples, the samples were supplemented with 1 mM DTT (Sigma) prior to centrifugation and at all subsequent steps.

Quantifying Phase Separation In Vitro. WT and mutant CTD variants were desalted into MES Buffer and diluted to 40 μM. Phase separation was initiated by adding an equal volume of MES Buffer supplemented with either 0, 75, 150, 300, 600, or 1,000 mM NaCl, resulting in final salt concentrations of 0, 37.5, 75, 150, 300, and 500 mM NaCl, respectively. Samples were mixed by gentle agitation and promptly centrifuged at 12,000 rpm for 10 min. The concentration of CTD in the supernatant was measured by A_{280} (E_{280} = 17,990 $M^{-1}{\cdot}cm^{-1}$) with a Nanodrop 2000c. All experiments were performed in triplicate.

Microscopy. WT and mutant CTD were desalted into MES Buffer and diluted to 40 μM. Phase separation was initiated by addition of an equal volume of MES Buffer supplemented with either 0 or 600 mM NaCl, resulting in final salt concentrations of 0 or 300 mM NaCl, respectively. Samples were spotted onto glass coverslips, and differential interference contrast (DIC) micrographs were acquired with a Zeiss Axiovert 200M as previously described (33). Images were processed with ImageJ.

Translational Diffusion. Translational diffusion coefficients of WT and mutant CTD were calculated by nonlinear least-squares fit of CH_3 ^{1}H spectral region intensity ratios to the Stejskal–Tanner equation (70):

$$\frac{I(g)}{I_0} = e^{-\gamma D\delta^2 g^2\left(\Delta-\frac{\delta}{3}\right)}, \quad [3]$$

where γ is the ^{1}H gyromagnetic ratio, D is the translational diffusion coefficient, δ is the length of the bipolar encoding/decoding gradient element, Δ is the diffusion time, and g is the gradient strength. SE in the diffusion coefficients was estimated from the variance–covariance matrix of nonlinear least-squares model parameters.

TDP-43$_{RRM\text{-}GFP}$ Reporter Assays. HEK-293T cells (ATCC catalog number CRL-3216; RRID:CVCL_0063) maintained in DMEM high glucose (GE Healthcare) supplemented with 10% FBS, 2 mM L-glutamine (Gibco), 1 mM nonessential amino acids (Gibco), and 1% penicillin/streptomycin (Gibco) at 37 °C and 5% CO_2 were seeded onto ibidi μ-slides at 30,000 cells per well and transfected with TDP-43$_{RRM\text{-}GFP}$ reporter constructs (300 ng) using X-tremeGENE 9 (Roche). After 24 h, the culture medium was exchanged with L-15 medium (Gibco) supplemented with 10% FBS, and the cells were imaged using a Leica SP8 laser-scanning confocal microscope equipped with a 488-nm laser, 63× glycerol objective (numerical aperture, 1.3) and a temperature-controlled incubation chamber (Life Imaging Services) set to 37 °C.

Half-bleach experiments were recorded and quantified using the FRAP module of the Leica Application Suite X software as previously described (35). In short, for each recorded time point (t), the fluorescence intensities within the bleached droplet hemisphere were then normalized to the fluorescence intensity of the corresponding unbleached droplet hemisphere. These normalized, time-dependent fluorescence intensities I_t were then used to calculate the fluorescence recovery (FR) according to the following formula: $FR(t) = (I_t - I_{t0})/(I_{before\ bleaching} - I_{t0})$, with t0 being the first time point observed after photobleaching. Two replicate experiments per construct were performed and at least 10 individual droplets from different cells were analyzed per experiment. Replicate measurements (mean ± SD) were plotted using GraphPad Prism. To ensure that only similarly sized droplets of comparable intensities were bleached, the same bleach window and detector settings were used. Droplet diameters and fluorescence intensities were quantified using Mathematica (Wolfram Research) as previously described (35).

Splicing Assays. WT and mutant siRNA-resistant constructs were generated by site-directed mutagenesis in N-terminally FLAG-tagged pCMV2 (71). HeLa cells were grown in growth media–DMEM, 4,500 mg/L glucose, L-glutamine, and sodium bicarbonate, and supplemented with filtered FBS at 10%. Cells were transiently transfected with Lipofectamine 2000 and Oligofectamine in the case of siRNA (Life Technologies) according to manufacturer protocols. RNA interference-mediated down-regulation of TDP-43 was carried out as previously described (71) and siCONTROL Nontargetting siRNA#1 (Dharmacon) was used as control. TDP-43 down-regulation was confirmed by immunoblotting. Splicing assays were performed using the CFTR reporter minigene as previously described (71). WT or mutant siRNA-resistant vectors were cotransfected in T2-treated cells. To quantify exon skipping, we performed standard PCR with primers specific for exon 9 flanking regions following RNA extraction and cDNA synthesis. The percent exon exclusion was calculated using ImageJ analysis.

All-Atom Simulations. Parallel tempering in the well-tempered ensemble (PT-WTE) simulations (72, 73) were conducted on a 41-residue fragment of TDP-43 CTD, TDP-43$_{310-350}$ using the GROMACS-4.6.7 molecular dynamics software package (74). We use the Amber03ws force field, which has been developed and parameterized for use with disordered proteins and protein folding (75). For simulations of WT TDP-43$_{310-350}$ dimer, we also apply a well-tempered metadynamics (WT-MetaD) bias (76) on two collective variables, intermolecular hydrophobic contacts and intermolecular hydrogen bonds, to aid in sampling bound and unbound states.

Coarse-Grained Simulations. Coarse-grained simulations were conducted using an amino acid-resolution model with 20 residue types to capture sequence specificity, having interactions based on relative hydropathies of each amino acid (56, 77). Each system was simulated at a range of temperatures using constant volume and temperature using a Langevin thermostat, and slab geometry, which allows for efficient sampling of coexistence densities. Simulations of phase coexistence were conducted using HOOMD-Blue v2.1.5 software package (78, 79). For simulations of helical TDP-43, residues 320–334 were constrained to a helical configuration using rigid-body dynamics.

Analysis of Simulations. Secondary structures were calculated using the DSSP algorithm (44), and secondary-structure maps are used to show heterogeneity of helicity within the equilibrium ensemble (45). From the PT-WTE-MetaD dimer simulation, we generate the free energy profile with respect to the two collective variables (80). All analysis done on the dimer simulation was reweighted based on the applied bias. Chemical shifts were calculated using SPARTA+ (81) and normalized using random-coil shifts from the Poulson webserver (62).

Data, Associated Protocols, Code, and Materials Availability. NMR chemical shift assignments in this paper for TDP-43 CTD G335A (27750), G335N (27788), G335S (27789), G338A (27790), and G335D (50090) can be obtained online from the Biological Magnetic Resonance Data Bank (BMRB) (http://www.bmrb.wisc.edu/). TDP-43 CTD WT chemical shifts were obtained from the BMRB (26823). Plasmids generated for this project can be found at Addgene.org. Associated protocols and simulation code can be obtained by contacting the corresponding authors.

ACKNOWLEDGMENTS. We thank Mandar Naik for assistance with NMR spectroscopy and Ashley Reeb for help with tissue culture and transfection experiments. Research at Brown University was supported in part by National Institute of General Medical Sciences (NIGMS) Grant R01GM118530 (to N.L.F.), NSF Grant 1845734 (to N.L.F.), and a starter grant 17-IIP-342 from the ALS Association (to N.L.F.). A.E.C. and A.M.D. were supported in part by NIGMS training grant to the Molecular Biology, Cell Biology, and Biochemistry (MCB) graduate program at Brown University (T32GM007601). G.L.D., G.H.Z., and J.M. are supported by the US Department of Energy (DOE), Office of Science, Basic Energy Sciences, Division of Material Sciences and Engineering under Award DESC0013979 (to J.M.). Work at Stanford University was supported by grants from the NIH (DP2GM105448 and R35GM118082) to R.R. and a fellowship from the Deutsche Forschungsgemeinschaft (SCHM 3082/2-1) to H.B.S. This research is based in part on data obtained at the Brown University Structural Biology Core Facility supported by the Division of Biology and Medicine, Brown University. Use of the high-performance computing capabilities of the Extreme Science and Engineering Discovery Environment, which is supported by NSF Grant TG-MCB-120014, is gratefully acknowledged in addition to resources of the National Energy Research Scientific Computing Center, a DOE Office of Science User Facility supported by the Office of Science of the US Department of Energy under Contract DE-AC02-05CH11231. The content is solely the responsibility of the authors and does not necessarily represent the official views of the funding agencies.

1. M. Kato *et al.*, Cell-free formation of RNA granules: Low complexity sequence domains form dynamic fibers within hydrogels. *Cell* **149**, 753–767 (2012).
2. D. M. Mitrea *et al.*, Nucleophosmin integrates within the nucleolus via multi-modal interactions with proteins displaying R-rich linear motifs and rRNA. *eLife* **5**, 1–33 (2016).
3. T. J. Nott *et al.*, Phase transition of a disordered nuage protein generates environmentally responsive membraneless organelles. *Mol. Cell* **57**, 936–947 (2015).
4. C. Brangwynne, C. Hoege, J. Gharakhani, F. Jülicher, A. A. Hyman, Germline P granules are liquid droplets that localize by controlled dissolution/condensation. *Science* **324**, 1729–1732 (2009).
5. A. A. Hyman, C. A. Weber, F. Jülicher, Liquid-liquid phase separation in biology. *Annu. Rev. Cell Dev. Biol.* **30**, 39–58 (2014).
6. C. P. Brangwynne, P. Tompa, R. V. Pappu, Polymer physics of intracellular phase transitions. *Nat. Phys.* **11**, 899–904 (2015).
7. S. Elbaum-Garfinkle *et al.*, The disordered P granule protein LAF-1 drives phase separation into droplets with tunable viscosity and dynamics. *Proc. Natl. Acad. Sci. U.S.A.* **112**, 7189–7194 (2015).
8. A. Molliex *et al.*, Phase separation by low complexity domains promotes stress granule assembly and drives pathological fibrillization. *Cell* **163**, 123–133 (2015).

9. A. Patel *et al*., A liquid-to-solid phase transition of the ALS protein FUS accelerated by disease mutation. *Cell* **162**, 1066–1077 (2015).
10. D. T. Murray *et al*., Structure of FUS protein fibrils and its relevance to self-assembly and phase separation of low-complexity domains. *Cell* **171**, 615–627.e16 (2017).
11. H. Cinar, S. Cinar, H. S. Chan, R. Winter, Pressure-induced dissolution and reentrant formation of condensed, liquid-liquid phase-separated elastomeric α-Elastin. *Chemistry* **24**, 8286–8291 (2018).
12. T. P. Dao *et al*., Ubiquitin modulates liquid-liquid phase separation of UBQLN2 via disruption of multivalent interactions. *Mol. Cell* **69**, 965–978.e6 (2018).
13. J. McCarty, K. T. Delaney, S. P. O. Danielsen, G. H. Fredrickson, J. E. Shea, Complete phase diagram for liquid-liquid phase separation of intrinsically disordered proteins. *J. Phys. Chem. Lett.* **10**, 1644–1652 (2019).
14. A. C. Murthy *et al*., Molecular interactions underlying liquid-liquid phase separation of the FUS low-complexity domain. *Nat. Struct. Mol. Biol.* **26**, 637–648 (2019).
15. R. M. Vernon *et al*., Pi-Pi contacts are an overlooked protein feature relevant to phase separation. *eLife* **7**, 1–48 (2018).
16. C. W. Pak *et al*., Sequence determinants of intracellular phase separation by complex coacervation of a disordered protein. *Mol. Cell* **63**, 72–85 (2016).
17. Y. Lin, D. S. W. Protter, M. K. Rosen, R. Parker, Formation and maturation of phase-separated liquid droplets by RNA-binding proteins. *Mol. Cell* **60**, 208–219 (2015).
18. Y.-H. Lin, H. S. Chan, Phase separation and single-chain compactness of charged disordered proteins are strongly correlated. *Biophys. J.* **112**, 2043–2046 (2017).
19. J. Amaya, V. H. Ryan, N. L. Fawzi, The SH3 domain of Fyn kinase interacts with and induces liquid-liquid phase separation of the low-complexity domain of hnRNPA2. *J. Biol. Chem.* **293**, 19522–19531 (2018).
20. P. Li *et al*., Phase transitions in the assembly of multivalent signalling proteins. *Nature* **483**, 336–340 (2012).
21. A. Wang *et al*., A single N-terminal phosphomimic disrupts TDP-43 polymerization, phase separation, and RNA splicing. *EMBO J.* **37**, e97452 (2018).
22. F. G. Quiroz, A. Chilkoti, Sequence heuristics to encode phase behaviour in intrinsically disordered protein polymers. *Nat. Mater.* **14**, 1164–1171 (2015).
23. S. Kroschwald *et al*., Different material states of Pub1 condensates define distinct modes of stress adaptation and recovery. *Cell Rep.* **23**, 3327–3339 (2018).
24. B. S. Schuster *et al*., Controllable protein phase separation and modular recruitment to form responsive membraneless organelles. *Nat. Commun.* **9**, 2985 (2018).
25. Y. H. Lin, J. P. Brady, J. D. Forman-Kay, H. S. Chan, Charge pattern matching as a "fuzzy" mode of molecular recognition for the functional phase separations of intrinsically disordered proteins. *New J. Phys.* **19**, 115003 (2017).
26. N. H. Alami *et al*., Axonal transport of TDP-43 mRNA granules is impaired by ALS-causing mutations. *Neuron* **81**, 536–543 (2014).
27. E. Bentmann *et al*., Requirements for stress granule recruitment of fused in sarcoma (FUS) and TAR DNA-binding protein of 43 kDa (TDP-43). *J. Biol. Chem.* **287**, 23079–23094 (2012).
28. C. Colombrita *et al*., TDP-43 is recruited to stress granules in conditions of oxidative insult. *J. Neurochem.* **111**, 1051–1061 (2009).
29. L. Liu-Yesucevitz *et al*., Tar DNA binding protein-43 (TDP-43) associates with stress granules: Analysis of cultured cells and pathological brain tissue. *PLoS One* **5**, e13250 (2010).
30. M. Neumann *et al*., Ubiquitinated TDP-43 in frontotemporal lobar degeneration and amyotrophic lateral sclerosis. *Science* **314**, 130–133 (2006).
31. T. Arai *et al*., TDP-43 is a component of ubiquitin-positive tau-negative inclusions in frontotemporal lobar degeneration and amyotrophic lateral sclerosis. *Biochem. Biophys. Res. Commun.* **351**, 602–611 (2006).
32. K. A. Josephs *et al*., Updated TDP-43 in Alzheimer's disease staging scheme. *Acta Neuropathol.* **131**, 571–585 (2016).
33. A. E. Conicella, G. H. Zerze, J. Mittal, N. L. Fawzi, ALS mutations disrupt phase separation mediated by α-helical structure in the TDP-43 low-complexity C-terminal domain. *Structure* **24**, 1537–1549 (2016).
34. L. Lim, Y. Wei, Y. Lu, J. Song, ALS-causing mutations significantly perturb the self-assembly and interaction with nucleic acid of the intrinsically disordered prion-like domain of TDP-43. *PLoS Biol.* **14**, e1002338 (2016).
35. H. B. Schmidt, R. Rohatgi, In vivo formation of vacuolated multi-phase compartments lacking membranes. *Cell Rep.* **16**, 1228–1236 (2016).
36. T. Afroz *et al*., Functional and dynamic polymerization of the ALS-linked protein TDP-43 antagonizes its pathologic aggregation. *Nat. Commun.* **8**, 45 (2017).
37. V. Romano, Z. Quadri, F. E. Baralle, E. Buratti, The structural integrity of TDP-43 N-terminus is required for efficient aggregate entrapment and consequent loss of protein function. *Prion* **9**, 1–9 (2015).
38. M. Mompeán *et al*., Point mutations in the N-terminal domain of transactive response DNA-binding protein 43 kDa (TDP-43) compromise its stability, dimerization, and functions. *J. Biol. Chem.* **292**, 11992–12006 (2017).
39. M. Mompeán *et al*., The TDP-43 N-terminal domain structure at high resolution. *FEBS J.* **283**, 1242–1260 (2016).
40. A. D'Ambrogio *et al*., Functional mapping of the interaction between TDP-43 and hnRNP A2 in vivo. *Nucleic Acids Res.* **37**, 4116–4126 (2009).
41. E. Buratti, TDP-43 post-translational modifications in health and disease. *Expert Opin. Ther. Targets* **22**, 279–293 (2018).
42. S. Roberts *et al*., Injectable tissue integrating networks from recombinant polypeptides with tunable order. *Nat. Mater.* **17**, 1154–1163 (2018).
43. L. Corrado *et al*., High frequency of TARDBP gene mutations in Italian patients with amyotrophic lateral sclerosis. *Hum. Mutat.* **30**, 688–694 (2009).
44. W. Kabsch, C. Sander, Dictionary of protein secondary structure: Pattern recognition of hydrogen-bonded and geometrical features. *Biopolymers* **22**, 2577–2637 (1983).
45. J. Iglesias, M. Sanchez-Martínez, R. Crehuet, SS-map: Visualizing cooperative secondary structure elements in protein ensembles. *Intrinsically Disord. Proteins* **1**, e25323 (2013).
46. J. W. Bryson *et al*., Protein design: A hierarchic approach. *Science* **270**, 935–941 (1995).
47. L. E. Kay, D. A. Torchia, A. Bax, Backbone dynamics of proteins as studied by 15N inverse detected heteronuclear NMR spectroscopy: Application to staphylococcal nuclease. *Biochemistry* **28**, 8972–8979 (1989).
48. M. Mompeán, A. Chakrabartty, E. Buratti, D. V. Laurents, Electrostatic repulsion governs TDP-43 C-terminal domain aggregation. *PLoS Biol.* **14**, e1002447 (2016).
49. C. R. Bodner, C. M. Dobson, A. Bax, Multiple tight phospholipid-binding modes of α-synuclein revealed by solution NMR spectroscopy. *J. Mol. Biol.* **390**, 775–790 (2009).
50. V. H. Ryan *et al*., Mechanistic view of hnRNPA2 low-complexity domain structure, interactions, and phase separation altered by mutation and arginine methylation. *Mol. Cell* **69**, 465–479.e7 (2018).
51. K. A. Burke, A. M. Janke, C. L. Rhine, N. L. Fawzi, Residue-by-residue view of in vitro FUS granules that bind the C-terminal domain of RNA polymerase II. *Mol. Cell* **60**, 231–241 (2015).
52. I. R. Mackenzie *et al*., TIA1 mutations in amyotrophic lateral sclerosis and frontotemporal dementia promote phase separation and alter stress granule dynamics. *Neuron* **95**, 808–816.e9 (2017).
53. J. Kyte, R. F. Doolittle, S. Diego, A simple method for displaying the hydropathic character of a protein. *J. Mol. Biol.* **157**, 105–132 (1982).
54. Z. Monahan *et al*., Phosphorylation of the FUS low-complexity domain disrupts phase separation, aggregation, and toxicity. *EMBO J.* **36**, 2951–2967 (2017).
55. G. L. Dignon, W. Zheng, R. B. Best, Y. C. Kim, J. Mittal, Relation between single-molecule properties and phase behavior of intrinsically disordered proteins. *Proc. Natl. Acad. Sci. U.S.A.* **115**, 9929–9934 (2018).
56. G. L. Dignon, W. Zheng, Y. C. Kim, R. B. Best, J. Mittal, Sequence determinants of protein phase behavior from a coarse-grained model. *PLOS Comput. Biol.* **14**, e1005941 (2018).
57. E. Buratti *et al*., Nuclear factor TDP-43 and SR proteins promote in vitro and in vivo CFTR exon 9 skipping. *EMBO J.* **20**, 1774–1784 (2001).
58. W. H. Landschulz, P. F. Johnson, S. L. McKnight The leucine zipper: A hypothetical structure common to a new class of DNA binding proteins. *Science* **240**, 1759–1764 (1988).
59. Y. Shin *et al*., Spatiotemporal control of intracellular phase transitions using light-activated optoDroplets. *Cell* **168**, 159–171.e14 (2017).
60. S. N. Ho, H. D. Hunt, R. M. Horton, J. K. Pullen, L. R. Pease, Site-directed mutagenesis by overlap extension using the polymerase chain reaction. *Gene* **77**, 51–59 (1989).
61. M. Kjaergaard, S. Brander, F. M. Poulsen, Random coil chemical shift for intrinsically disordered proteins: Effects of temperature and pH. *J. Biomol. NMR* **49**, 139–149 (2011).
62. M. Kjaergaard, F. M. Poulsen, Sequence correction of random coil chemical shifts: Correlation between neighbor correction factors and changes in the Ramachandran distribution. *J. Biomol. NMR* **50**, 157–165 (2011).
63. C. D. Kroenke, J. P. Loria, L. K. Lee, M. Rance, A. G. Palmer, Longitudinal and transverse ^{1}H-^{15}N dipolar/^{15}N chemical shift anisotropy relaxation interference: Unambiguous determination of rotational diffusion tensors and chemical exchange effects in biological macromolecules. *J. Am. Chem. Soc.* **120**, 7905–7915 (1998).
64. D. H. Wu, A. Chen, C. S. Johnson, An improved diffusion-ordered spectroscopy experiment incorporating bipolar-gradient pulses. *J. Magn. Reson. A* **115**, 260–264 (1995).
65. M. Holz, H. Weingartner, Calibration in accurate spin-echo self-diffusion measurements using ^{1}H and less-common nuclei. *J. Magn. Reson.* **92**, 115–125 (1991).
66. F. Delaglio *et al*., NMRPipe: A multidimensional spectral processing system based on UNIX pipes. *J. Biomol. NMR* **6**, 277–293 (1995).
67. W. Lee, M. Tonelli, J. L. Markley, NMRFAM-SPARKY: Enhanced software for biomolecular NMR spectroscopy. *Bioinformatics* **31**, 1325–1327 (2015).
68. C. Wang, M. J. Grey, A. G. Palmer, 3rd, CPMG sequences with enhanced sensitivity to chemical exchange. *J. Biomol. NMR* **21**, 361–366 (2001).
69. P. R. McIntosh, R. B. Freedman, Characteristics of a copper-dependent cross-linking reaction between two forms of cytochrome P-450 in rabbit-liver microsomal membranes. *Biochem. J.* **187**, 227–237 (1980).
70. E. O. Stejskal, J. E. Tanner, Spin diffusion measurements: Spin echoes in the presence of a time-dependent field gradient. *J. Chem. Phys.* **42**, 288–292 (1965).
71. W. Li *et al*., Heat shock-induced phosphorylation of TAR DNA-binding protein 43 (TDP-43) by MAPK/ERK kinase regulates TDP-43 function. *J. Biol. Chem.* **292**, 5089–5100 (2017).
72. G. Bussi, F. L. Gervasio, A. Laio, M. Parrinello, Free-energy landscape for β hairpin folding from combined parallel tempering and metadynamics. *J. Am. Chem. Soc.* **128**, 13435–13441 (2006).
73. M. Deighan, M. Bonomi, J. Pfaendtner, Efficient simulation of explicitly solvated proteins in the well-tempered ensemble. *J. Chem. Theory Comput.* **8**, 2189–2192 (2012).
74. B. Hess, C. Kutzner, D. van der Spoel, E. Lindahl, E. Lindahl, GROMACS 4: Algorithms for highly efficient, load-balanced, and scalable molecular simulation. *J. Chem. Theory Comput.* **4**, 435–447 (2008).
75. R. B. Best, W. Zheng, J. Mittal, Balanced protein-water interactions improve properties of disordered proteins and non-specific protein association. *J. Chem. Theory Comput.* **10**, 5113–5124 (2014).
76. A. Barducci, G. Bussi, M. Parrinello, Well-tempered metadynamics: A smoothly converging and tunable free-energy method. *Phys. Rev. Lett.* **100**, 1–4 (2008).
77. Y. C. Kim, G. Hummer, Coarse-grained models for simulations of multiprotein complexes: Application to ubiquitin binding. *J. Mol. Biol.* **375**, 1416–1433 (2008).
78. J. A. Anderson, C. D. Lorenz, A. Travesset, General purpose molecular dynamics simulations fully implemented on graphics processing units. *J. Comput. Phys.* **227**, 5342–5359 (2008).
79. J. Glaser *et al*., Strong scaling of general-purpose molecular dynamics simulations on GPUs. *Comput. Phys. Commun.* **192**, 97–107 (2015).
80. M. Bonomi, A. Barducci, M. Parrinello, Reconstructing the equilibrium Boltzmann distribution from well-tempered metadynamics. *J. Comput. Chem.* **30**, 1615–1621 (2009).
81. Y. Shen, A. Bax, SPARTA+: A modest improvement in empirical NMR chemical shift prediction by means of an artificial neural network. *J. Biomol. NMR* **48**, 13–22 (2010).